

# Bloch Point Quadrupole Constituting Hybrid Topological Strings Revealed with Electron Holographic Vector Field Tomography

Fehmi Sami Yasin,\* Jan Masell, Yoshio Takahashi, Tetsuya Akashi, Norio Baba, Kosuke Karube, Daisuke Shindo, Takahisa Arima, Yasujiro Taguchi, Yoshinori Tokura, Toshiaki Tanigaki, and Xiuzhen Yu\*

Topological magnetic (anti)skyrmions are robust string-like objects heralded as potential components in next-generation topological spintronics devices due to their low-energy manipulability via stimuli such as magnetic fields, heat, and electric/thermal current. While these 2D topological objects are widely studied, intrinsically 3D electron-spin real-space topology remains less explored despite its prevalence in bulky magnets. 2D-imaging studies reveal peculiar vortex-like contrast in the core regions of spin textures present in antiskyrmion-hosting thin plate magnets with  $S_4$  crystal symmetry, suggesting a more complex 3D real-space structure than the 2D model suggests. Here, holographic vector field electron tomography captures the 3D structure of antiskyrmions in a single-crystal, precision-doped  $(\text{Fe}_{0.63}\text{Ni}_{0.3}\text{Pd}_{0.07})_3\text{P}$  (FNPP) lamellae at room temperature and zero field. These measurements reveal hybrid string-like solitons composed of skyrmions with topological number  $W = -1$  on the lamellae's surfaces and an antiskyrmion ( $W = +1$ ) connecting them. High-resolution images uncover a Bloch point quadrupole (four magnetic (anti)monopoles that are undetectable in 2D imaging) which enables the observed lengthwise topological transitions. Numerical calculations corroborate the stability of hybrid strings over their conventional (anti)skyrmion counterparts. Hybrid strings result in topological tuning, a tunable topological Hall effect, and the suppression of skyrmion Hall motion, disrupting existing paradigms within spintronics.

## 1. Introduction

Magnetic (anti)skyrmions,<sup>[1–4]</sup> which cause the topological Hall effect and exhibit current-driven Hall motion, are highly desirable solitons due to their topological protection and their manipulability via low-energy stimuli including magnetic fields,<sup>[5–8]</sup> heat,<sup>[6,9]</sup> and electric/thermal current.<sup>[10–16]</sup> One of the origins of these spin textures lies within the competition between the ferromagnetic exchange interaction and the Dzyaloshinskii–Moriya interaction (DMI).<sup>[6,17]</sup> The former concerns the force on each spin to align with its neighbors, whereas the latter is an antisymmetric exchange interaction between neighboring spins that favors spin canting away from parallel alignment. The resulting real space textures are now well-known in 2D. Bloch-type skyrmions (Figure 1a,b) are proper screw-like spin propagations with cores pointing up/down embedded in a background of opposite orientation, and exhibit either clockwise or counterclockwise vortex-like in-plane

F. S. Yasin, J. Masell, K. Karube, D. Shindo, T. Arima, Y. Taguchi, Y. Tokura, X. Yu

RIKEN Center for Emergent Matter Science (CEMS)

RIKEN, Wako 351-0198, Japan

E-mail: fehmi.yasin@riken.jp; yu\_x@riken.jp

J. Masell

Institute of Theoretical Solid State Physics

Karlsruhe Institute of Technology (KIT)

76049 Karlsruhe, Germany

 The ORCID identification number(s) for the author(s) of this article can be found under <https://doi.org/10.1002/adma.202311737>

© 2024 The Authors. Advanced Materials published by Wiley-VCH GmbH. This is an open access article under the terms of the [Creative Commons Attribution](#) License, which permits use, distribution and reproduction in any medium, provided the original work is properly cited.

DOI: 10.1002/adma.202311737

Y. Takahashi, T. Akashi, T. Tanigaki  
Research and Development Group  
Hitachi Ltd.

Hatoyama 350–0395, Japan

N. Baba

Research Institute for Science and Technology

Kogakuin University

Hachioji 192-0015, Japan

T. Arima

Department of Advanced Materials Science

University of Tokyo

Kashiwa 277–8561, Japan

Y. Tokura

Department of Applied Physics

University of Tokyo

Tokyo 113–8656, Japan

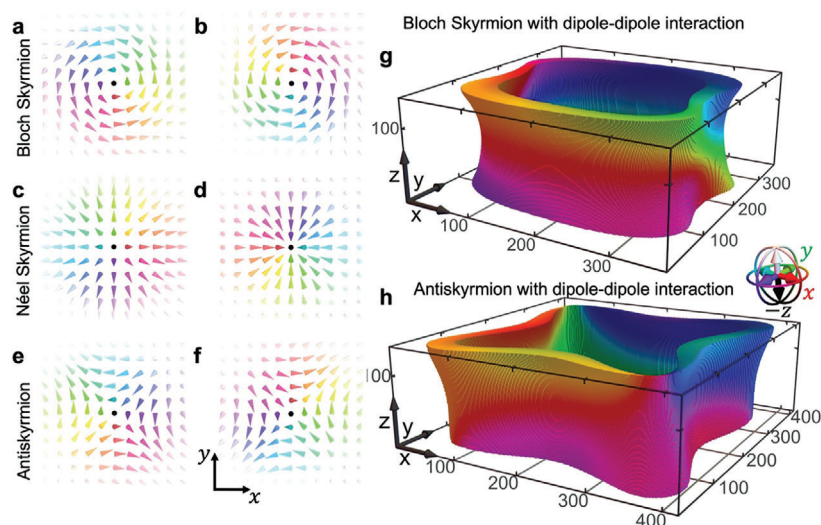


**Figure 1.** Real-space structure of skyrmions and antiskyrmions. a,b) Bloch-type skyrmions with topological number  $W = -1$  and helicity a)  $\gamma = \pi/2$  and b)  $\gamma = -\pi/2$ . c,d) Néel-type skyrmions with topological charge  $W = -1$  and helicity c)  $\gamma = 0$  and d)  $\gamma = \pi$ . e,f) Antiskyrmions with topological charge  $W = +1$  and helicity e)  $\gamma = -\pi/2$  and f)  $\gamma = \pi/2$ . g,h) In-plane magnetization ( $|m_z| < 1/6$ ) of ideal g) skyrmion and h) antiskyrmion strings stabilized using micromagnetic simulations including dipole–dipole interactions. The axis labels are in units of length (nm).

structure. They contrast with Néel-type skyrmions (Figure 1c,d) composed of cycloidal spin propagations twisting radially inward or outward from their core spins. Skyrmions of both types are characterized by an integer topological number  $W = \frac{1}{4\pi} \int \int \mathbf{m} \times \left( \frac{\partial \mathbf{m}}{\partial x} \times \frac{\partial \mathbf{m}}{\partial y} \right) dx dy = -1$ , where  $\mathbf{m} = \frac{\mathbf{M}}{|\mathbf{M}|}$  is the normalized magnetization.<sup>[12]</sup> On the other hand, antiskyrmions (Figure 1e,f) have an in-plane antivortex magnetic structure, that is, the nature of their domain walls alternate between Bloch and Néel-type. The four Néel-type regions are typically termed Bloch lines<sup>[4,6,18]</sup> and the spin texture exhibits  $W = +1$ .

Recent results have confirmed that in 3D, skyrmions are string-like objects.<sup>[7,8,19–26]</sup> Furthermore, dipole–dipole energy can stabilize hybrid skyrmion strings<sup>[27–31]</sup> composed of Néel-type skyrmion surface layers linked via a Bloch-type skyrmion (simulated in-plane magnetization, defined as the region where  $|m_z| < 1/6$ , is shown in Figure 1g), and predicted to have lower velocities and skyrmion Hall angles than their 2D counterparts.<sup>[16,28]</sup> The idea for Néel-type domain wall twists near sample surfaces was introduced over fifty years ago in magnetic bubble-hosting uniaxial ferromagnets.<sup>[32,33]</sup> It can be understood from the demagnetization field  $\mu_0 \mathbf{H}_{\text{demag}}(\mathbf{r})$  generated to cancel the magnetic surface and volume charges,

$$\mathbf{B}_{\text{demag}}(\mathbf{r}) = \mu_0 \mathbf{H}_{\text{demag}}(\mathbf{r}) = -\nabla \left( \frac{1}{4\pi} \left[ \int \frac{\rho_V(\mathbf{r}')}{|\mathbf{r} - \mathbf{r}'|} dV' + \int \frac{\sigma_s(\mathbf{r}')}{|\mathbf{r} - \mathbf{r}'|} dS' \right] \right) \quad (1)$$

where  $\rho_V = -(\nabla \times \mathbf{M}(\mathbf{r}))$  is the reduced volume charge density and  $\sigma_s = \mathbf{M}(\mathbf{r}) \times \mathbf{n}$  is the surface charge density, where  $\mathbf{n}$  is the surface normal. The in-plane component of  $\mathbf{B}_{\text{demag}}(\mathbf{r})$  perpendicular to domain walls increases substantially near the surface, torquing the magnetic bubbles' domain wall magnetization field to be entirely Néel-like for some depth below the surface.<sup>[34]</sup>

In  $D_{2d}$  and  $S_4$  crystal symmetry magnets, DMI is anisotropic, leading to the formation of antiskyrmions, skyrmions, and nontopological bubbles.<sup>[4,6,17,35]</sup> Moreover, dipole–dipole interactions combine with anisotropic DMI to form characteristic square-shaped antiskyrmions.<sup>[6]</sup> In  $(\text{Fe}_{0.63}\text{Ni}_{0.3}\text{Pd}_{0.07})_3\text{P}$ , (anti)skyrmions were observed to have a vortex-like magnetic field configuration within their cores,<sup>[17]</sup> suggesting a more complex 3D structure than the 2D model assumes. Micromagnetic simulations including demagnetization suggest the Bloch regions of an antiskyrmion's domain walls twist Néel-type near the surfaces (Figure 1h), deforming the spin texture: the Bloch-type regions widen while the Bloch line magnetizations (four corners of Figure 1h) widen on one surface and narrow on the other.

Recent work has also revealed controlled transformations between topological skyrmions and antiskyrmions via nontopological bubbles.<sup>[6,36]</sup> Such transformations are enabled by micromagnetic structures called (anti)Bloch points (BPs), which are singularities in the magnetization with (anti)hedgehog structure (Figure 2b–e). These magnetic monopoles have been predicted to play a role in magnetization dynamics including its reversal in soft ferromagnets,<sup>[37]</sup> pinning to the atomic lattice,<sup>[38]</sup> domain wall dynamics,<sup>[39]</sup> skyrmion lattice annihilation<sup>[40]</sup> and vortex core reversal.<sup>[41]</sup> BPs have also been found to reduce the total energy of a thin film sample when present within a singular Bloch line that switches its orientation along the sample.<sup>[42,43]</sup> While (anti)BPs have been observed in real space using both X-rays<sup>[21,44,45]</sup> and electrons,<sup>[7]</sup> their detailed 3D structure has yet

Y. Tokura  
Tokyo College  
University of Tokyo  
Tokyo 113–8656, Japan

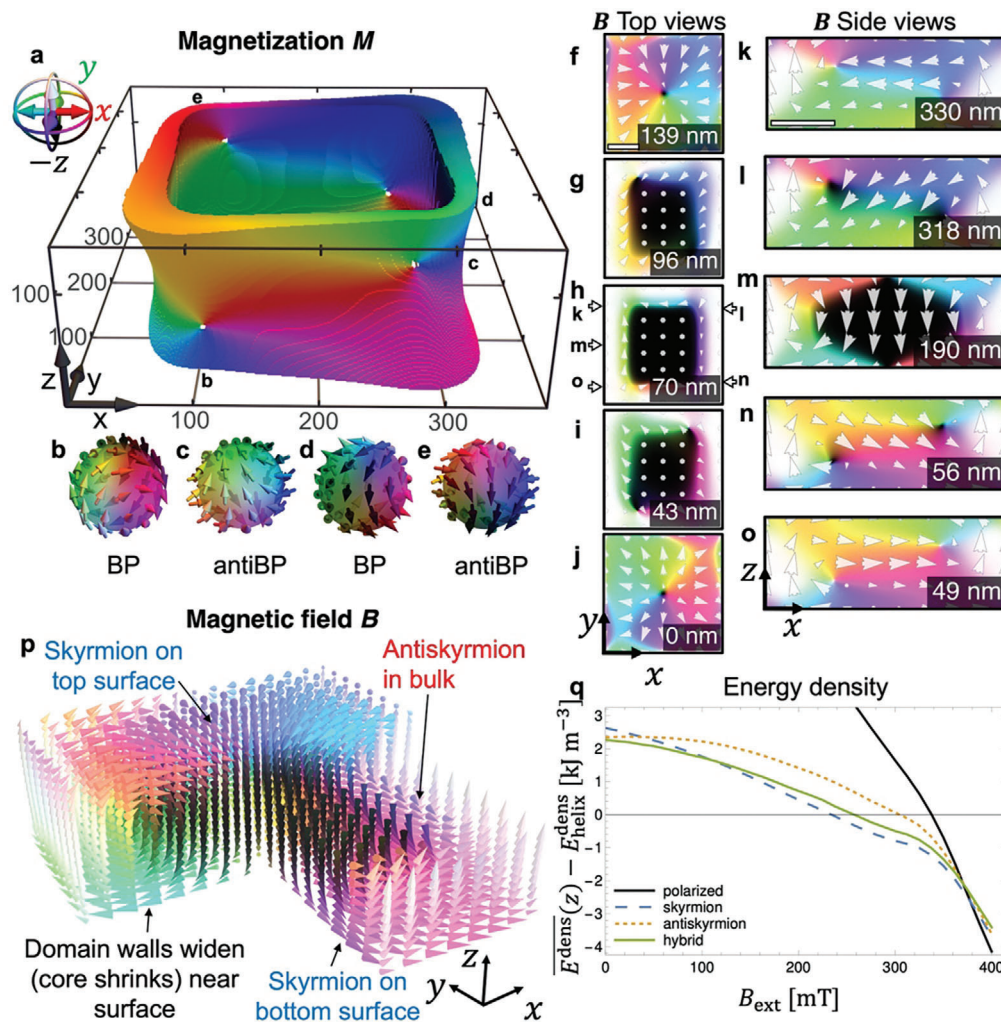


**Figure 2.** Hybrid antiskyrmion strings and their 3D features. a) Isosurface depicting the in-plane magnetization ( $|m_z| < 1/6$ ) of a micromagnetically simulated hybrid antiskyrmion string with a thickness 140 nm and optimized energy density. The axis labels are in units of length (nm). b–e) BPs and antiBPs indicated in (a) magnified with both color and glyph plots. These points indicate the depth from the surface at which the hybrid antiskyrmion string topologically transitions from a skyrmion at the surface to an antiskyrmion in the bulk. f–j)  $xy$ -slices of the hybrid antiskyrmion string's magnetic field  $B$  at f)  $z = 139$  nm, g) 96 nm, h) 70 nm, i) 43 nm and j) 0 nm. k–o)  $xz$ -slices of the hybrid antiskyrmion string's magnetic field at k)  $y = 330$  nm, l) 318 nm, m) 190 nm, n) 56 nm and o) 49 nm. p) 3D glyph plot of  $B$  with selected regions omitted to show cross-sections of the bulk of the spin texture simultaneously with the surface. q) Energy density as a function of magnetic field  $B_{\text{ext}}$ , respectively. The hybrid solution is the first excited below a critical field threshold, outperforming ideal (anti)skyrmions. Scalebars in (f,k) are 100 nm.

to be measured in high resolution. Similarly, hybrid topological spin textures have yet to be confirmed experimentally via real-space 3D imaging.

In this work, we use off-axis electron holography configured for vector field electron tomography (VFET)<sup>[22,46–48]</sup> to image a hybrid antiskyrmion string (Figure 2a) in an FNPP nanoplate at room temperature and zero field. These 3D measurements unveil four (anti)BPs located along the antiskyrmion's Bloch lines and arranged in a quadrupole, enabling a topological transformation from skyrmion at the surfaces to antiskyrmion in the bulk. Furthermore, energy density calculations of these hybrid strings suggest that the dipolar and DMI energy terms are leading contributors in stabilizing topologically complex hybrid strings over their ideal counterparts.

## 2. Results

### 2.1. Stabilization of Hybrid Strings in FNPP

Hybrid strings naturally stabilize as the lowest energy density nontrivial topological spin texture when relaxing an antiskyrmion state using micromagnetic simulations with FNPP parameters.<sup>[17,35]</sup> As shown in Figure 2a, the in-plane magnetization depicts a domain wall twisting from Néel-type skyrmions on the surfaces to antiskyrmion in the center. To enable this transition, (anti-)BPs form near the antiskyrmion's four corners: two BPs near the bottom surface transforming the skyrmion into an antiskyrmion (Figure 2b,d), and two antiBPs near the top surface transforming the antiskyrmion into a skyrmion (Figure 2c,e). This topological transition is also illustrated in

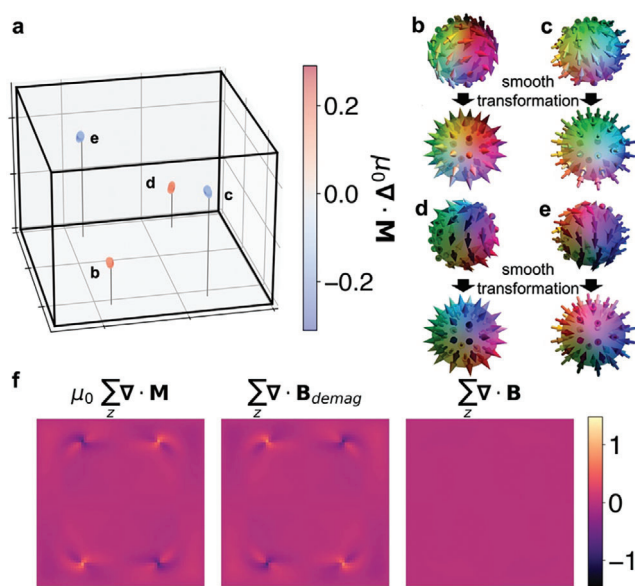


**Figure 3.** Detailed 3D structure of the simulated magnetization of the BP quadrupole. a) 3D divergence of the magnetization,  $\mu_0 \nabla \times \mathbf{M}$ . The data points where  $\nabla \times \mathbf{M} < (\nabla \times \mathbf{M})^{\max}/2.5$  are omitted for ease of visibility of the (anti)BP structure. b–e) BPs (b,d) and antiBPs (c,d) indicated in a magnified with both color and glyph plots. The upper panels show the simulated magnetizations as shown in Figure 2b–e in the main text, while the lower panels show the same spins smoothly transformed (all spins rotated smoothly, holding the topology constant) while keeping the same color to easily track the spins, revealing the topological equivalence of these (anti)BPs with (anti)hedgehogs. The divergence in a also confirms this equivalence, with  $\nabla \times \mathbf{M} > 0$  for BPs and  $\nabla \times \mathbf{M} < 0$  for antiBPs, respectively. f, Plots of  $\mu_0 \sum_z \nabla \times \mathbf{M}$ ,  $\sum_z \nabla \times \mathbf{B}_{\text{demag}}$ , and  $\sum_z \nabla \times \mathbf{B}$  from left to right, respectively, confirming the (anti)BP quadrupole constituting these hybrid spin textures.

the magnetic vector field  $\mathbf{B}(\mathbf{r}) = \mu_0 \mathbf{M}(\mathbf{r}) + \mathbf{B}_{\text{demag}}(\mathbf{r})$  slices shown in Figure 2f–j ( $xy$ -plane view) and Figure 2k–o ( $xz$ -plane view). Here, the skyrmions orient radially inward on top (Figure 2f) and outward on bottom (Figure 2j), minimizing the magnetostatic (dipole–dipole) energy by closing the magnetic field lines running along the spin texture’s core and periphery.

The 3D magnetic field of a hybrid string is shown in Figure 2p, indicating another feature of note: the shrinking of the core near the surfaces and corresponding expansion of the domain wall’s width consistent with the combination of weak uniaxial anisotropy and strong dipole–dipole interaction characteristic of FNPP. The positions of the four (anti)BPs are indicated by dashed black crosses in the right-hand-side (RHS) panel of Figure S1a (Supporting Information), which shows the center slice of  $\mathbf{B}(\mathbf{r})$ . Figure S1b–e (Supporting Information) plot  $xz$ - and  $yz$ -slices of  $\mathbf{B}(\mathbf{r})$  intersecting the (anti)BP positions side-by-side with the magnitude of  $\mathbf{B}(\mathbf{r})$  versus  $z$  along the Bloch lines which host the (anti)BPs. Notably,  $|\mathbf{B}(\mathbf{r})|$  decreases to a minimum at the (anti)BP position. This is because  $\mathbf{M}(\mathbf{r})$  has a non-zero divergence  $\nabla \cdot \mathbf{M}(\mathbf{r})$  at the (anti)BPs, as shown in Figure 3a.  $\nabla \cdot \mathbf{M}(\mathbf{r}) > 0$  for the BPs and  $\nabla \cdot \mathbf{M}(\mathbf{r}) < 0$  for the antiBPs, indicating that the magnetization field is source- and sink-like at those points, respectively. To illustrate this, we performed a smooth transformation on the

BPs shown in the top panels of Figure 3b,d and antiBPs in the top panels of Figure 3c,e while conserving the topological number, resulting in the hedgehogs and anti-hedgehogs shown in the bottom panels. The nonzero  $\nabla \times \mathbf{M}(\mathbf{r})$  at the (anti)BP quadrupole generates a nonzero  $\nabla \times \mathbf{B}_{\text{demag}}(\mathbf{r})$ , resulting in  $\nabla \times \mathbf{B}(\mathbf{r}) = 0$  (Figure 3f) and decrease in  $|\mathbf{B}(\mathbf{r})|$ .

The anisotropy ( $E_{\text{ani}}/V$ ), dipolar ( $E_{\text{dd}}/V$ ), exchange ( $E_{\text{ex}}/V$ ), DMI ( $E_{\text{dmi}}/V$ ), and total ( $E_{\text{tot}}/V$ ) volume energy densities are plotted as functions of  $z$  for hybrid, antiskyrmion, and skyrmion strings in Figure 4a–c, respectively. The gray-shaded thickness region in Figure 4a indicates  $W = +1$ , while the neighboring regions have  $W = -1$ . The (anti)BPs are located where  $W$  changes sharply from skyrmion-like ( $W = -1$ ) to antiskyrmion-like ( $W = +1$ ) on the top surface (antiBPs) and vice versa on the bottom surface (BPs). At these singular points,  $E_{\text{tot}}/V$  rises sharply due to the exchange interaction but decreases on the surfaces when compared to  $E_{\text{tot}}/V$  of an ideal antiskyrmion string due to the skyrmion-like surface spin textures that satisfy the flux loop closure desired by dipolar interactions. Note that ideal antiskyrmion strings never fully optimize this interaction as their in-plane antivortex character always comprises regions with moments pointing inward and outward. A comparison of the energy densities of hybrid strings (solid green), skyrmion strings (dashed blue), and antiskyrmion strings (dotted orange) are plotted as a function of  $z$  in Figure 4d. On the other hand, anisotropic DMI favors a bulk antiskyrmion, and so  $E_{\text{tot}}/V$  of the hybrid string is lower than the ideal skyrmion in this region.

$E_{\text{tot}}/V$  of hybrid strings (solid green) is lower than skyrmion (dashed blue) and antiskyrmion strings (dotted orange), as well as the polarized state (solid black) at a low magnetic field ( $\mathbf{B}_{\text{ext}}$ ) values including zero field, as shown in Figure 2q. Notably,  $E_{\text{tot}}/V$  of ideal antiskyrmion strings remains higher than that of hybrid strings for all  $\mathbf{B}_{\text{ext}}$  values. As we will discuss later, the introduction of  $\mathbf{B}_{\text{ext}}$  changes the  $z$ -location of the (anti)BPs, resulting in a tunable thickness-averaged topological number  $\bar{W}$ . We plot  $\bar{W}(\mathbf{B}_{\text{ext}})$  in Figure 4e for the polarized/helical state (solid black line), ideal skyrmion string (dashed blue line), ideal antiskyrmion string (dotted orange line), and hybrid string (solid green line). Figure S2 (Supporting Information) shows a comparison of the in-plane magnetic induction between the skyrmion (Figure S2a–c, Supporting Information), antiskyrmion (Figure S2d–f, Supporting Information), and hybrid string (Figure S2g–i, Supporting Information) at the top (Figure S2a,d,g, Supporting Information), middle (Figure S2b,e,h, Supporting Information), and bottom (Figure S2c,f,i, Supporting Information) of the spin textures. The decrease in energy from both the skyrmion capping layers and decreased bulk shape deformation compensates for the energy increase at the (anti)BPs, stabilizing the hybrid string.

## 2.2. Imaging Magnetic Monopoles

We prepared a metastable hybrid string within an FNPP square-tipped nanoplate (Figure S3a,b, see Experimental Section, Supporting Information for details). We used off-axis electron holography VFET (experimental geometry outlined in Figure S4, Supporting Information) to acquire holograms at tilt angles along two tilt axes over a range of  $360^\circ$  in  $5^\circ$  steps. We followed the procedure described in Table S1 (Supporting Information) to extract

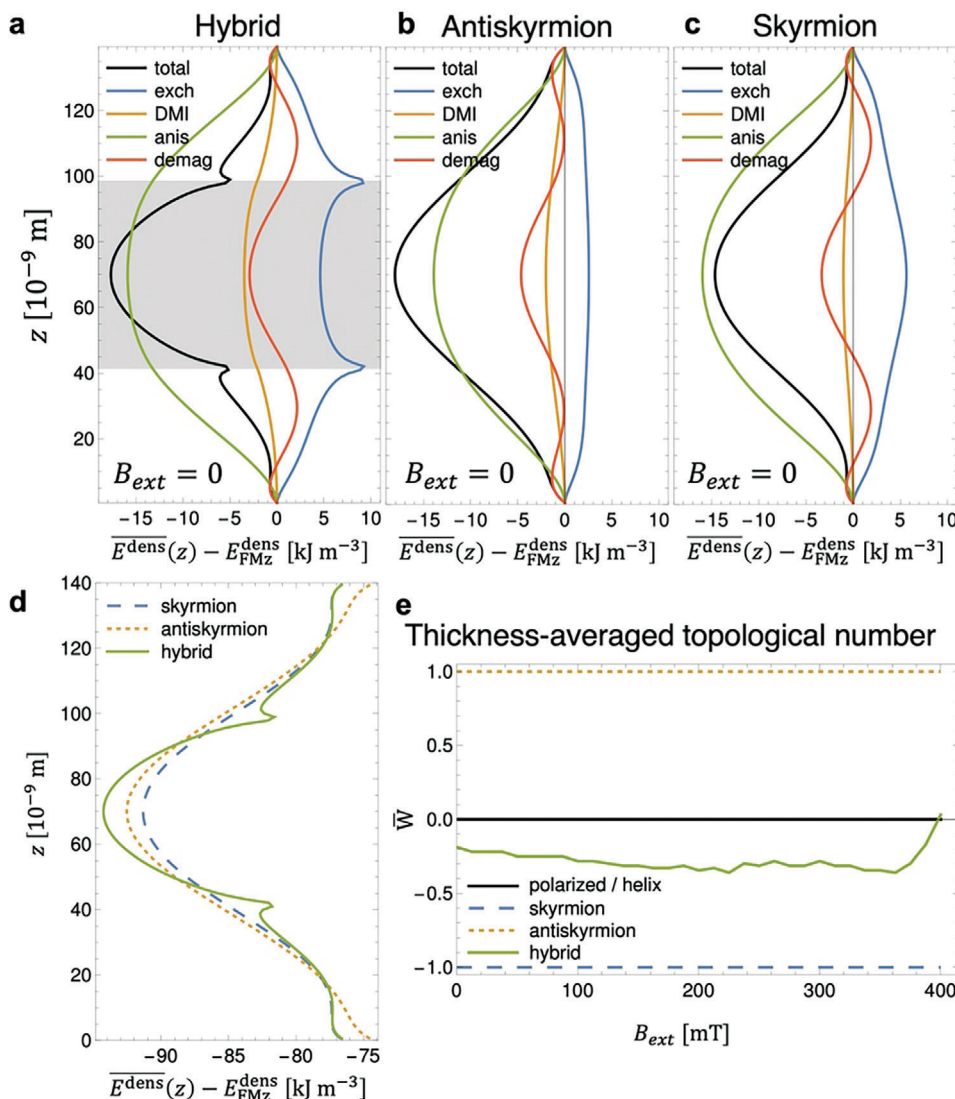


**Figure 4.** Detailed comparison between hybrid antiskyrmion strings and ideal (anti)skyrmion strings. (a–c), Total volume energy density  $E_{tot}/V$ , exchange energy density  $E_{ex}/V$ , DMI energy density  $E_{DMI}/V$ , uniaxial anisotropy energy density  $E_{ani}/V$ , and dipole–dipole energy density  $E_{dd}/V$  as a function of  $z$  for a) hybrid antiskyrmion strings, b) ideal antiskyrmion strings, and c) ideal skyrmion strings. The gray-shaded thickness region in a indicates  $W = +1$ , while the neighboring regions above and below indicate  $W = -1$ . d) Total volume energy density  $E/V$  at  $B_{ext} = 0$  as a function of the penetration depth  $z$  (on the  $y$ -axis). The hybrid antiskyrmion string solution gains energy (density) in the bulk like an antiskyrmion and at the surfaces like a skyrmion but has an energy penalty in the topological transition region where the BPs are located. e) Thickness-averaged topological number as a function of magnetic field  $B_{ext}$ , respectively. The topology of ideal skyrmion and antiskyrmion strings is non-trivial but well-defined,  $+1$  or  $-1$  throughout the sample. In contrast, hybrid antiskyrmion strings have a non-integer average topological number which depends on the external magnetic field and other energy contributions.

the magnetic phase along every tilt angle at which the electron beam could penetrate through the sample without a significant loss of beam coherence due to inelastic scattering events, resulting in a  $130^\circ$  tilt angle range along both tilt axes. We reconstructed the 3D magnetic field using the recently developed quantization units reconstruction technique (QURT). QURT does not require a priori knowledge of the 3D structure and provides higher resolution and smaller  $z$ -elongation caused by a missing wedge of tilt angles when compared to other reconstruction algorithms.<sup>[49,50]</sup>

The resulting reconstruction of  $\mathbf{B}(\mathbf{r})$  in the region of the hybrid string is presented in Figure 5. As predicted in the previously described simulations, the transition from skyrmion on

the top surface to antiskyrmion in the bulk to skyrmion on the bottom surface is clearly seen in the  $xy$ -plane slices shown in Figure 5a–c. Furthermore, this topological transformation occurs at distinct  $z$ -slices containing (anti)BPs, two of which are circled in Figure 5d,e. The  $xz$ - and  $yz$ -planes that intersect at the Bloch line along which the (anti)BP circled in Figure 5d is located are plotted using 3D glyphs in the RHS panel. The magnitude of  $\mathbf{B}(\mathbf{r})$  along the Bloch line (Figure 5f) decreases to nearly zero at the anti-BP, in agreement with the previously described simulations. The locations of the other (anti)BPs (circled in black) may also be seen from the vortex-like whirls on either side of the downward-oriented core spins shown in Figure 5g,h, which are

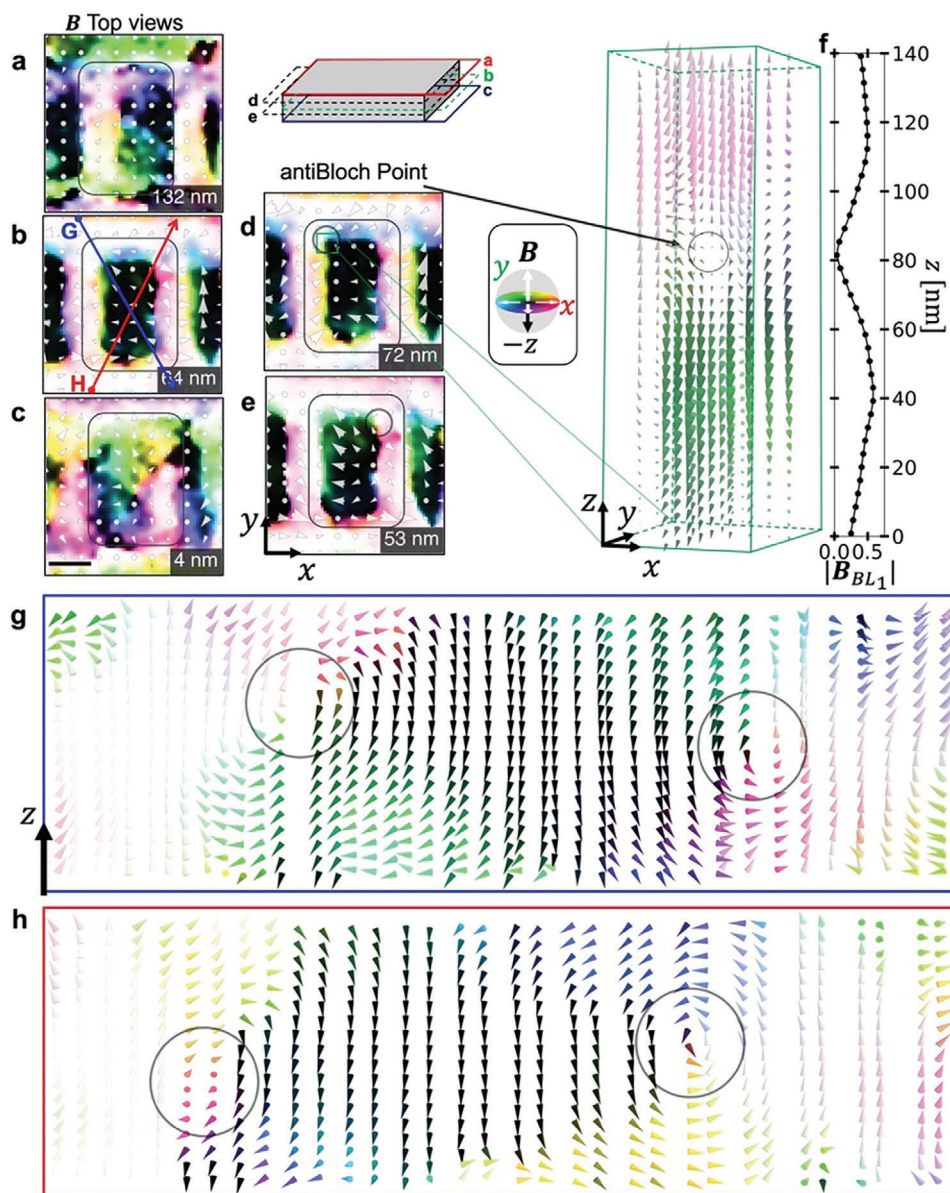


**Figure 5.** Experimental vector field tomography reconstruction of a hybrid antiskyrmion string in  $(\text{Fe}_{0.63}\text{Ni}_{0.3}\text{Pd}_{0.07})_3\text{P}$ . a–e)  $xy$ -slices of the experimentally measured 3D magnetic field at a)  $t = 132$  nm, b) 64 nm, c) 4 nm showing the surface skyrmions a,c) and bulk antiskyrmion (b), respectively, as well as at d)  $t = 79$  nm and e) 53 nm which indicate the spatial positions of the (anti)BPs (circled with a solid black line) where the spin texture transforms topologically from skyrmion to antiskyrmion and vice-versa. The colors display the orientation of the experimentally measured 3D vector field as mapped by the 3D color map outlined by the black rectangle in between (d,f) whereas the arrows' length represents the magnitude of the in-plane projection of the 3D magnetic field. The spin texture is outlined by a solid dark grey rectangle in (a–e). The right-hand-side inset plots the magnetic field in the  $xz$ - and  $yz$ -planes intersecting the antiBP indicated by a solid green square in (d). f) Plot of the magnitude of the magnetic field measured along the Bloch line ( $|B_{BL1}|$ ) as a function of  $z$ . g,h) Glyph plots of the normalized magnetic field along the Bloch lines within the sliced planes (intersecting the  $xy$ -plane) indicated by blue (g) and red (h) rectangles in (b). The (anti)BP locations are circled in solid black. The scalebar in (c) is 100 nm.

slices selected to intersect two (anti)BPs simultaneously along the hybrid string's diagonals indicated in Figure 5b. The length of the arrows/glyphs in Figure 5a–e corresponds to  $|B(r)|$ , whereas  $B(r)$  is normalized in Figure 5g,h to increase overall visibility. Curiously,  $B(r)$  does not whirl in a vortex-like texture within the displayed plane around the (anti)BP on the left-hand-side (LHS) of Figure 5h, but instead rotates within the  $xy$ -plane down the  $z$ -direction.

We plot the detailed structure of the experimentally measured magnetic field  $B(r)$  around all four (anti)BPs in Figure 6. The  $xy$  locations of the (anti)BPs are marked by transparent blue squares in the in-plane  $B(r)$  map shown in Figure 6a as  $BP_1$ ,  $BP_2$ ,  $BP_3$ , and  $BP_4$ , respectively. The 3D location of this BP quadrupole is revealed in Figure 6b, which plots the 3D topological charge density  $\rho_w$ . The topological charge density increases substantially near the BP locations, and the sign reverses along the  $z$ -direction at

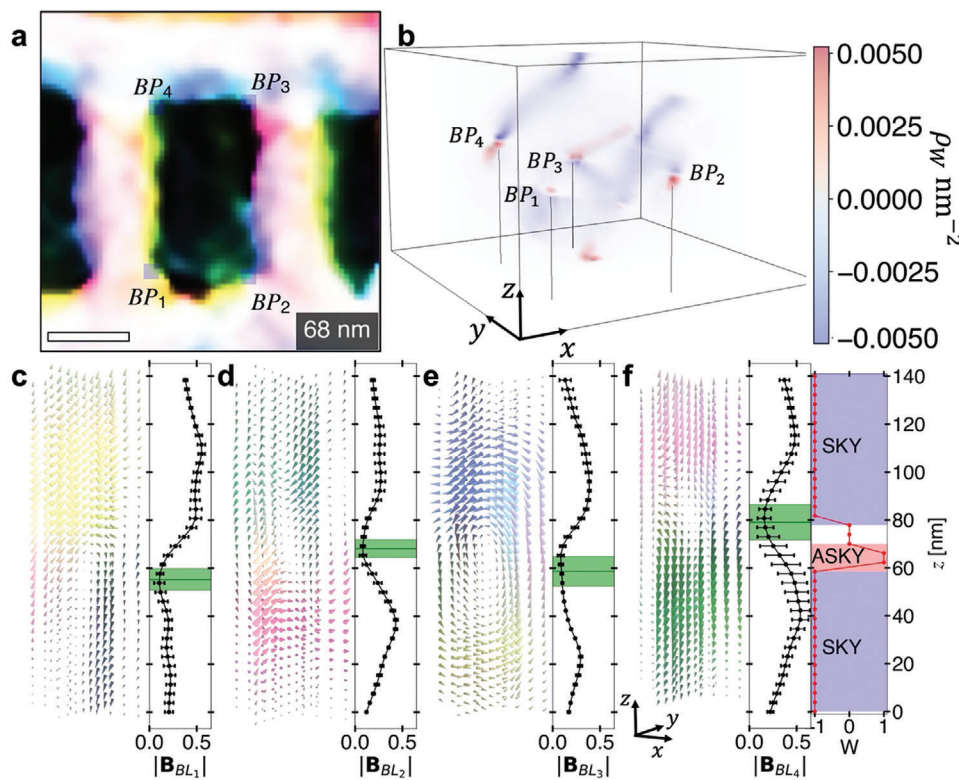


**Figure 6.** Experimentally measured 3D structure of  $B(z)$  along the Bloch lines of a zero-field hybrid antiskyrmion string. a)  $xy$ -slice through the center of the thickness with the approximate  $xy$ -location of the (anti)BPs indicated by the shaded blue box, scale bar 100 nm. b) 3D plot of the topological charge density  $\rho_W$ . The (anti)BP positions are labeled and indicated by the gray lines drawn from the BPs to the  $z = 0$  plane. c–f)  $xz$ - and  $yz$ -slices of  $B$  intersecting the (anti)BPs positioned at the  $xy$  locations indicated by the shaded blue regions in a plotted side-by-side with the magnitude of  $B$  versus  $z$  averaged over the  $xy$ -locations indicated in the shaded blue box in (a), with the error bars representing the standard deviation from the mean. The solid green line represents the  $z$  location of the minimum magnitude of  $B$  averaged over the  $xy$ -locations indicated in the shaded blue box in (a),  $|B|_{\min}(z)$ , which may be thought of as the locations of the (anti)BPs. The  $xy$ -locations where  $|B|_{\min}(z) > (|B|_{\min}(z) + 0.1)$  were omitted from the average calculation and the shaded green region indicates the standard deviation from the mean. The right-hand-side of (f) is a plot of the topological charge  $W$  versus  $z$ . The skyrmion and antiskyrmion thickness regions are shaded in blue and red, respectively.

the BP. The  $xz$ - and  $yz$ -planes of  $B(r)$  intersecting the (anti)BPs positioned at the  $xy$  locations indicated by the shaded blue regions in (a) are plotted in Figure 6c–f side-by-side with the magnitude of  $B(r)$  versus  $z$  averaged over the  $xy$ -locations within the shaded blue box in (a), with the error bars representing the standard deviation from the mean. The solid green line represents the  $z$  location of the minimum magnitude of  $B(r)$  averaged over the  $xy$ -locations indicated in the shaded blue box in (a),  $|B|_{\min}(z)$ , which may be thought of as the locations of the (anti)BPs. The  $xy$ -locations where  $|B|_{\min}(z) > (|B|_{\min}(z) + 0.1)$  were omitted from the average calculation and the shaded green region indicates the standard deviation from the mean. The topological charge  $W$  is plotted as a function of  $z$  to the right of Figure 6f, illustrating the substantial skyrmion surface layers measured here.

In addition to a 3D plot of normalized  $B(r)$  in Figure 7, we plot a slice of the magnetic field dissecting the rectangular hybrid string's long axis in the upper RHS panel using glyphs superimposed on a color plot of the core spins defined as the region in which the  $z$  component of the measured magnetic field  $B_z(r) < -0.2$ . The thin plate's surfaces are indicated on the top and bottom of

the slice, and the domain walls are outlined with dashed blue and red lines on the LHS and RHS, respectively. We plot the core area per slice in the upper RHS panel of Figure 7. The hybrid string's core area shrinks near the surfaces, corresponding to an increase in the domain walls' width, to minimize dipolar energy. The core area of the antiskyrmion portion of the spin texture (the  $z$ -center region) is the largest region, with the core's lateral contraction occurring in the skyrmion portions of the spin texture, suggesting that skyrmions are quite malleable, consistent with recent studies on skyrmion deformation.<sup>[15,27]</sup>

The distance of the BPs from the surfaces can be qualitatively understood by simple geometric arguments. At the surfaces, magnetostatic energy is minimized by forming Landau domain structures that close the magnetic flux within the material, that is, the single-handedness Néel domain walls on the surfaces that form skyrmions are in fact circular in-plane magnetic domains enabled by the very low uniaxial anisotropy of FNPP. The angle between the domain wall separating the up/down domains in the bulk and the domain wall separating the bulk and surface domains is roughly at  $45^\circ$  which conserves magnetic flux. Thus, in this limit, the penetration depth of the Landau surface

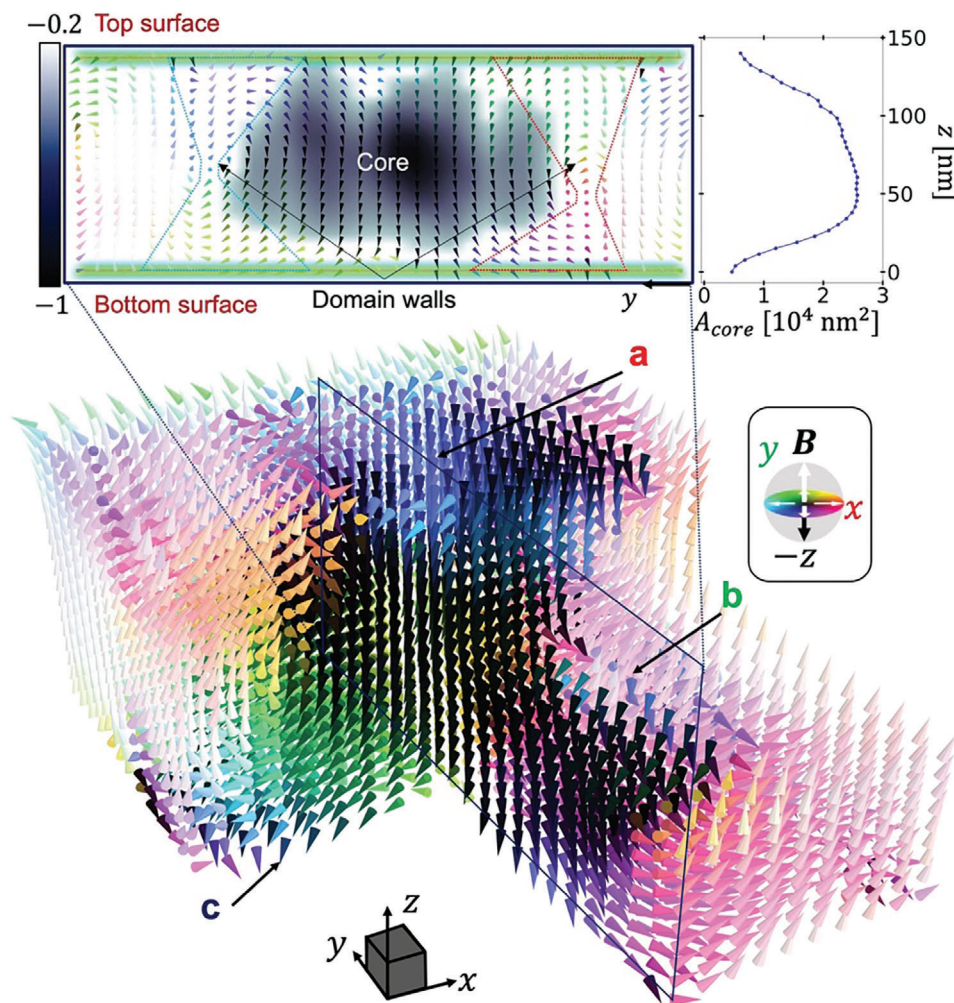


**Figure 7.** Experimentally measured 3D spin structure of a hybrid antiskyrmion string. Lower: 3D glyphs of the normalized magnetic field binned to 33 voxels per dimension and with the front-left and upper-front-right regions removed for visibility purposes. The top, middle, and bottom slices are marked with (a–c), respectively, corresponding to Figure 3a–c. A cube is drawn for scale in the bottom left with dimensions  $20 \times 20 \times 20 \text{ nm}^3$ . Upper left: Cross-sectional slice (outlined by a dark blue rectangle) of the normalized magnetic field with the domain walls of the hybrid antiskyrmion string roughly outlined in light blue and red and with the normalized spin texture core magnetic induction shaded (defined as  $B_z < -0.2$ ). Upper right: Area of the core spins  $A_{\text{core}}$  ( $\text{nm}^2$ ), plotted as a function of  $z$  (nm).

domains, which form the Néel skyrmion caps and thus indicate the topological transition point where the BPs are located, is half the distance between adjacent domain walls. This simple estimate is in good agreement with the experimental and numerical observations and also suggests a critical sample thickness, below which only skyrmions are stable.

### 2.3. Complex Topology of Hybrid Strings

A  $z$ -dependent topological charge leads to various consequences for a hybrid string's stability, dynamics, and 2D projection as measured via conventional magnetic imaging techniques. First, the existence of (anti)BPs begs the question whether their  $z$ -location can be controlled, and our micromagnetic simulation re-

sults suggest they can indeed be moved via  $B_{\text{ext}}$ , and ultimately eject from the thin plate for a large  $B_{\text{ext}}$ . More interestingly, this implies that  $\bar{W}$  may vary in a controlled way. Such a topological tuning would significantly alter the hybrid string's electric or thermal current-induced dynamics due to the magnus force, the force perpendicular to the driving current direction ( $F \parallel x$ ), which causes the so-called skyrmion Hall motion. For example, the magnus force in 2D models results in a velocity component perpendicular to the driving force,  $v_y \propto W$ . If we extend this into 3D and assume that the spin texture is rigid during motion,

we can expect  $v_y \propto \frac{1}{t} \int_0^t W(z) dz$ , where  $W(z)$  is the  $z$ -dependent topological charge and  $t$  is the sample thickness. We anticipate a comparable impact on transport measurements, as the topological Hall effect (THE) also varies with  $W$ . In other words,

hybrid antiskyrmion-hosting materials with a small characteristic domain width and large saturation magnetization may exhibit a tunable THE through changes in thickness,  $B_{\text{ext}}$ , or both.

The ability to tune a spin texture's transverse motion or a device's THE signal by simply changing  $B_{\text{ext}}$  or sample thickness would have wide-reaching impacts in spintronics and transport, respectively. Moreover, this Hall motion and THE signal can be eliminated altogether with the right combination of sample thickness and  $B_{\text{ext}}$ , as suggested by Figure 4e. Notably,  $\overline{W} \approx -0.11$  for a hybrid string at zero field, which may be interpreted as the skyrmion regions occupying 60% of the spin texture's length, with the other 40% being an antiskyrmion. As  $B_{\text{ext}}$  increases, the spin texture becomes more skyrmion-like as the (anti)BPs penetrate deeper into the bulk of the sample until some threshold field  $B_{\text{ext}} \approx 320$  mT, above which the trend reverses. This is also reflected in the energy density of each spin texture plotted in Figure 2q, where the antiskyrmion string's energy density decreases at a higher rate than both the skyrmion string and hybrid string for large, increasing  $B_{\text{ext}}$ . We therefore propose an experiment investigating the current-driven motion of hybrid strings and predict that for thin ( $t \leq 140$  nm) plate devices, hybrid strings exhibit skyrmion-like Hall motion for a wide range of applied magnetic fields, and that the motion may be tuned toward antiskyrmion-like using thicker devices or materials with a stronger anisotropic DMI.

#### 2.4. Bloch Twists in the Hybrid Strings' Skyrmion Layers

Finally, let us turn our attention to the hybrid string's 2D projection and signal as measured via conventional magnetic imaging methods such as Lorentz transmission electron microscopy<sup>[17,51]</sup> and differential phase contrast scanning transmission electron microscopy (DPC-STEM).<sup>[17,18]</sup> As mentioned in the introduction, spin textures intrinsic to FNPP often exhibit vortex-like contrast in their core regions. Representative LTEM and DPC-STEM micrographs illustrating this phenomenon are shown in Figure S5a,b (Supporting Information). To explain the formation mechanism, we integrated the 3D magnetic field obtained via micromagnetic simulations of a hybrid string lattice stabilized in a 125 mT external field and plot it in Figure S5c (Supporting Information). Vortex-like magnetic structure emerges in the hybrid strings' core region, which is clearly seen in the magnified image of the center hybrid string in Figure S5d (Supporting Information) along with the 1D profiles of the horizontal and vertical plotted in Figure S5e,f (Supporting Information), respectively.

The real-space structure of hybrid strings can explain this phenomenon as follows. The vortex cores are a result of the hybridization of the two skyrmion caps on the surfaces which partially twist from Néel to Bloch type as a function of distance from the surface. To minimize exchange energy, the Bloch-type winding, whose handedness is energetically degenerate, spontaneously breaks this symmetry and chooses the same handedness on either surface. The spontaneously chosen handedness comes hand in hand with a rectangular deformation of the otherwise square-shaped hybrid antiskyrmion. The elongation axis of the rectangular hybrid antiskyrmion thus likely correlates with the handedness of the projected vortex, potentially enabling control over the vortex handedness or distortion by tuning its conjugate

partner. Because the hybrid string's domain walls expand near the surface as previously discussed and shown in Figure 7, the vortex contrast appears as if inside of the spin textures' core region in 2D imaging. As shown in the lower-middle hybrid antiskyrmion, a square shape results in the suppression of the vortex contrast, corresponding to a much weaker Bloch component of the skyrmion capping layers.

### 3. Conclusion

In this work, we used holographic VFET to reveal the 3D structure of an (anti)BP quadrupole constituting a zero-field, room-temperature hybrid antiskyrmion string. We performed this imaging months after stabilizing the spin texture in the FNPP nanoplate, demonstrating its long lifetime and robust metastability. Another intriguing research direction is what becomes of the (anti)BPs upon application of an electric/thermal current. These topological transition points may act as pinning defects that must be overcome, or perhaps they eject from the system upon application of a driving current. Either way, these points are essential for the construction of hybrid strings and require further study.

### 4. Experimental Section

**Sample Preparation:** Single-crystalline bulk samples of  $(\text{Fe}_{0.63}\text{Ni}_{0.3}\text{Pd}_{0.07})_3\text{P}$  were synthesized by a self-flux method from pure Fe, Ni, and Pd metals and red phosphorous sealed in an evacuated quartz tube. The target phase of tetragonal  $\text{M}_3\text{P}$  was isolated from the ingot. The phase purity of the  $\text{M}_3\text{P}$  structure was confirmed by powder X-ray diffraction with  $\text{Cu K}\alpha$  radiation.<sup>[17]</sup> Crystal orientations were checked by an X-ray Laue diffraction method. Chemical compositions were examined by a scanning electron microscope equipped with an energy-dispersive X-ray analyzer.<sup>[17]</sup>

**Nanoplate Fabrication:** The authors performed focused ion beam (FIB) lift out using the Thermo Scientific Helios 5 UX DualBeam. After lifting out a 3  $\mu\text{m}$  thin plate onto a TEM Cu half-moon-shaped mesh, the plate was thinned to  $\approx 500$  nm, then rotated the sample  $90^\circ$  to cut the desired plank shape with a  $1 \mu\text{m} \times 1 \mu\text{m}$  square end. A square-tipped sample geometry was chosen to help stabilize the target square-shaped antiskyrmions.<sup>[51]</sup> The sample was transferred to a 3D needle via FIB liftout for mounting in a TEM sample holder capable of  $360^\circ$  tilting. The sample  $-90^\circ$  was rotated to its original position to thin the plate to the desired thickness. After the final fabrication, a 5 keV ion beam was used to polish the two flat surfaces to remove any Ga implantation that might have occurred. After polishing, the final thickness was measured using the scanning electron microscope to be  $t \approx 140$  nm, as shown in Figure S3b (Supporting Information). Because the nanoplate was very small ( $\approx 1 \mu\text{m}^2$  in area as shown in Figure S3a, Supporting Information), the FIB could cut the sample to have a very flat profile, as evidenced by the straight line along the sample's side profile. The only place that featured some rounding was the edge itself, but the spin texture was located sufficiently far away ( $>100$  nm) from the edge so as not to experience the varying thickness there.

**Antiskyrmion Creation Procedure:** The sample was transferred to a 3D needle via FIB liftout for mounting in a TEM sample holder capable of  $360^\circ$  tilting. A magnetic field  $B_{\text{ext}} \approx 115$  mT was applied along the (001) crystal axis and field cooled from 410 to 295 K to create a metastable mixed spin texture lattice composed of mostly antiskyrmions, but also including some skyrmions and non-topological bubbles. The field was decreased to zero, after which several spin textures remained metastable, including the single antiskyrmion embedded in a helical background shown in Figure S3c (Supporting Information). FIB was then used to lift out

the nanoplank and attach it to a Hitachi TEM tomography holder needle capable of 360° tilting along two perpendicular axes. The antiskyrmion remained metastable in the nanoplank for months after transferring to the needle and before performing 3D imaging, highlighting the long lifetime of the spin texture.

**Holographic Vector Field Electron Tomography:** Holographic vector field electron tomography was performed in a 1 MV Hitachi holography electron microscope<sup>[52]</sup> and configured a double-biprism experimental setup<sup>[53]</sup> to achieve high-precision phase measurements. In off-axis electron holography, a plane wave of electrons is transmitted through the sample while a portion of the incident wave travels through a vacuum as a reference wave. The beam was then split by a Möllenstedt electrostatic biprism, biased such that the sample and reference waves were sufficiently phase-shifted to form a hologram at the camera, from which the sample phase might be reconstructed.

**Micromagnetic Simulations:** For the theoretical analysis, the same micromagnetic (continuum) model was considered and parameters as determined at  $T = 300$  K in Ref. [17]. The energy functional  $E(\mathbf{m}) = \int \epsilon(\mathbf{m}) dV$  comprised the magnetic stiffness  $A_{\text{ex}} = 8.1 \text{ pJ m}^{-1}$ , an  $S_4$ -symmetric Dzyaloshinskii-Moriya interaction (DMI)  $D = 0.2 \text{ mJ m}^{-2}$  which favors right-handed Bloch-type domain walls or helices in the  $x$ -direction and left-handed ones in the  $y$ -direction, uniaxial anisotropy  $K_u = 31 \text{ kJ m}^{-3}$ , the Zeeman interaction with an external field  $B_{\text{ext}}$ , and the demagnetizing field  $\mathbf{B}_{\text{demag}}(\mathbf{r})$  due to the saturation magnetization  $M_s = 417 \text{ kA m}^{-1}$ . Note that the real space data presented in this study depicts a 90° rotated sample to match the visualization of the experimental data. Explicitly, the energy density reads:

$$E[\mathbf{m}] = A(\nabla\mathbf{m})^2 + D[\mathbf{m} \cdot (\hat{x} \times \partial_x\mathbf{m}) - \mathbf{m} \cdot (\hat{y} \times \partial_y\mathbf{m})] - K_u(\mathbf{m} \cdot \hat{z})^2 - \mathbf{m} \cdot B_{\text{ext}} - \frac{M_s}{2}\mathbf{m} \cdot \mathbf{B}_{\text{demag}} \quad (2)$$

The modified version of MuMax3<sup>[54]</sup> was used to relax initial guesses for the magnetization texture and thereby find local energy minima of the energy  $E(\mathbf{m})$ . The modifications which was applied to MuMax3 include the specific form of the DMI and an upgrade for the discretization of derivatives, which in the code were approximated by higher-order finite difference schemes which involved more neighboring sites, as previously used in Refs. [7, 17, 35]. This results in slightly higher runtimes but much improved numerical accuracy (except very close to the Bloch points (BP) where the numerical error does not improve with this approach).

To minimize the energy density of the various magnetic phases, that is, i) helices, ii) skyrmions, iii) antiskyrmions, and iv) hybrid (anti)skyrmions, these textures were initialized on a numerical lattice with  $256 \times 256 \times 128$  lattice sites which yielded very high numerical accuracy. The lattice constant in the  $z$ -direction was chosen such that the thickness was 140 nm to match the experimentally measured specimen thickness. The boundary conditions were periodic in the  $x$ - and  $y$ -direction and von-Neumann (open) in the  $z$ -direction, using MuMax3's built-in function `setPBC(16,16,0)`. For a given value of the magnetic field  $B_{\text{ext}} = 0, 50, 100, \dots, 400$  mT the initial textures were optimized in independent simulations using `relax()` for different system sizes  $L_x = L_y = 250, 260, 270, \dots, 600$  nm. The energy density  $E^{\text{dens}} \equiv E/L_x L_y L_z = E/V$  (energy per volume) for every system size was then obtained by subtracting the energy of the  $z$ -polarized state from the energy of the relaxed state and dividing by the respective system size. The states with the lowest energy density were considered the thermodynamic ground states in this effective  $T = 0$  model and their energy densities were compared in Figure S3D (Supporting Information). For the calculation of the topological number, the lattice version was used by Berg and Lüscher.<sup>[55]</sup>

It was noted that the singular BP configurations, by definition, violated the assumption of smoothly varying magnetization underlying the continuum approximation in the micromagnetic model. However, the physical error was probably small as the dominant energy contributions came from the magnetization around the BP which was distorted on the length

scales of the micromagnetic model. Moreover, it was checked that the numerical error was small by comparing the simulation results of ideal BPs to the analytical solution for the case of only magnetic stiffness. Another possible issue arising from BPs on a numerical lattice was artificial pinning. This was indeed problematic as the hybrid textures might initialize with BPs which during the relaxation procedure were subject to pinning forces on the lattice. It was checked that this effect was small by initializing hybrid antiskyrmion strings with various values for the thickness of the skyrmion surface caps. Different initial cap thicknesses did not alter the final cap thickness very much. Moreover, it was found that these surface caps also naturally appeared in many simulations when the initial state was a homogeneous antiskyrmion string, underlining that the formation of the cap states was a robust mechanism. However, it was also realized that the fine numerical mesh chosen for the final plots in this study further increased the mobility of the BPs on the numerical lattice. In previous tests with two times lower numerical resolution and significantly faster runtimes, it was found that hybrid antiskyrmion strings tend to remain in the  $S_4$ -symmetric state in which they were created, that was, the antiskyrmions stayed square-shaped. Upon decreasing the lattice constants, it was found that the BPs become sufficiently mobile to allow for spontaneous symmetry breaking toward rectangular antiskyrmions due to the pair-wise attraction of BPs on distinct interfaces.

## Supporting Information

Supporting Information is available from the Wiley Online Library or from the author.

## Acknowledgements

The authors were very grateful to Tomoko Kikitsu (Materials Characterization Support Team in the RIKEN Center for Emergent Matter Science) for technical support on the TEM (JEM-2100F), as well as Ilya Belopolski, Max Hirschberger, Max Birch, and Naoto Nagaosa for helpful discussions. Y.T. acknowledges the support of the Japan Science and Technology Agency (JST) CREST program (Grant Number JPMJCR1874). X.Z.Y. acknowledges the support of Grants-In-Aid for Scientific Research (A) (Grant No. 19H00660) from JSPS and the JST-CREST program (Grant No. JP-MJCR20T1). J.M. was supported by the Alexander von Humboldt Foundation as a Feodor Lynen Return Fellow.

## Conflict of Interest

The authors declare no conflict of interest.

## Data Availability Statement

The raw data will be available in a public repository (figshare) upon publication of the article. We will provide the URL/DOI if the article proceeds to publication.

## Keywords

3D topology, antiskyrmions, Bloch points, electron holography, hybrid strings, Lorentz transmission electron microscopy, skyrmions

Received: November 6, 2023

Revised: December 22, 2023

Published online:

- [1] A. N. Bogdanov, D. A. Yablonskii, *Zh. Eksp. Teor. Fiz.* **1989**, 95, 178.
- [2] S. Mühlbauer, B. Binz, F. Jonietz, C. Pfleiderer, A. Rosch, A. Neubauer, R. Georgii, P. Böni, *Science* **2009**, 323, 915.
- [3] X. Z. Yu, Y. Onose, N. Kanazawa, J. H. Park, J. H. Han, Y. Matsui, N. Nagaosa, Y. Tokura, *Nature* **2010**, 465, 901.
- [4] A. K. Nayak, V. Kumar, T. Ma, P. Werner, E. Pippel, R. Sahoo, F. Damay, U. K. Rößler, C. Felser, S. S. P. Parkin, *Nature* **2017**, 548, 561.
- [5] L. Peng, F. S. Yasin, T. E. Park, S. J. Kim, X. Zhang, T. Nagai, K. Kimoto, S. Woo, X. Yu, *Adv. Funct. Mater.* **2021**, 31, 2103583.
- [6] L. Peng, R. Takagi, W. Koshibae, K. Shibata, K. Nakajima, T. hisa Arima, N. Nagaosa, S. Seki, X. Yu, Y. Tokura, *Nat. Nanotechnol.* **2020**, 15, 181.
- [7] X. Yu, J. Masell, F. S. Yasin, K. Karube, N. Kanazawa, K. Nakajima, T. Nagai, K. Kimoto, W. Koshibae, Y. Taguchi, N. Nagaosa, Y. Tokura, *Nano Lett.* **2020**, 20, 7313.
- [8] N. Mathur, F. S. Yasin, M. J. Stolt, T. Nagai, K. Kimoto, H. Du, M. Tian, Y. Tokura, X. Yu, S. Jin, *Adv. Funct. Mater.* **2021**, 31, 2008521.
- [9] X. Z. Yu, K. Shibata, W. Koshibae, Y. Tokunaga, Y. Kaneko, T. Nagai, K. Kimoto, Y. Taguchi, N. Nagaosa, Y. Tokura, *Phys. Rev. B* **2016**, 93, 134417.
- [10] T. Schulz, R. Ritz, A. Bauer, M. Halder, M. Wagner, C. Franz, C. Pfleiderer, K. Everschor, M. Garst, A. Rosch, *Nat. Phys.* **2012**, 8, 301.
- [11] X. Z. Yu, N. Kanazawa, W. Z. Zhang, T. Nagai, T. Hara, K. Kimoto, Y. Matsui, Y. Onose, Y. Tokura, *Nat. Commun.* **2012**, 3, 988.
- [12] N. Nagaosa, Y. Tokura, *Nat. Nanotechnol.* **2013**, 8, 899.
- [13] K. Litzius, I. Lemesch, B. Krüger, P. Bassirian, L. Caretta, K. Richter, F. Büttner, K. Sato, O. A. Tretiakov, J. Förster, R. M. Reeve, M. Weigand, I. Bykova, H. Stoll, G. Schütz, G. S. D. Beach, M. Kläui, *Nat. Phys.* **2017**, 13, 170.
- [14] X. Yu, F. Kagawa, S. Seki, M. Kubota, J. Masell, F. S. Yasin, K. Nakajima, M. Nakamura, M. Kawasaki, N. Nagaosa, Y. Tokura, *Nat. Commun.* **2021**, 12, 5079.
- [15] F. S. Yasin, J. Masell, K. Karube, A. Kikkawa, Y. Taguchi, Y. Tokura, X. Yu, *Proc. Natl. Acad. Sci. U. S. A.* **2022**, 119, e2200958119.
- [16] E. Raimondo, E. Saugar, J. Barker, D. Rodrigues, A. Giordano, M. Carpentieri, W. Jiang, O. Chubykalo-Fesenko, R. Tomasello, G. Finocchio, *Phys. Rev. Appl.* **2022**, 18, 024062.
- [17] K. Karube, L. Peng, J. Masell, X. Yu, F. Kagawa, Y. Tokura, Y. Taguchi, *Nat. Mater.* **2021**, 20, 335.
- [18] F. S. Yasin, L. Peng, R. Takagi, N. Kanazawa, S. Seki, Y. Tokura, X. Yu, *Adv. Mater.* **2020**, 32, 2004206.
- [19] S. Schneider, D. Wolf, M. T. J. Stolt, S. Jin, D. Pohl, B. Rellinghaus, M. Schmidt, B. Büchner, S. T. B. Goennenwein, K. Nielsch, A. Lubk, *Phys. Rev. Lett.* **2018**, 120, 217201.
- [20] S. Zhang, G. Van Der Laan, J. Müller, L. Heinen, M. Garst, A. Bauer, H. Berger, C. Pfleiderer, T. Hesjedal, *Proc. Natl. Acad. Sci. U. S. A.* **2018**, 115, 6386.
- [21] M. T. Birch, D. Cortés-Ortuño, L. A. Turnbull, M. N. Wilson, F. Groß, N. Träger, A. Laurensen, N. Bukin, S. H. Moody, M. Weigand, G. Schütz, H. Popescu, R. Fan, P. Steadman, J. A. T. Vezzhak, G. Balakrishnan, J. C. Loudon, A. C. Twitchett-Harrison, O. Hovorka, H. Fangohr, F. Y. Ogrin, J. Gräfe, P. D. Hatton, *Nat. Commun.* **2020**, 11, 1726.
- [22] D. Wolf, S. Schneider, U. K. Rößler, A. Kovács, M. Schmidt, R. E. Dunin-Borkowski, B. Büchner, B. Rellinghaus, A. Lubk, *Nat. Nanotechnol.* **2022**, 17, 250.
- [23] F. N. Rybakov, A. B. Borisov, S. Blügel, N. S. Kiselev, *Phys. Rev. Lett.* **2015**, 115, 117201.
- [24] F. Zheng, F. N. Rybakov, A. B. Borisov, D. Song, S. Wang, Z. A. Li, H. Du, N. S. Kiselev, J. Caron, A. Kovács, M. Tian, Y. Zhang, S. Blügel, R. E. Dunin-Borkowski, *Nat. Nanotechnol.* **2018**, 13, 451.
- [25] X. Yu, K. V. Iakoubovskii, F. S. Yasin, L. Peng, K. Nakajima, S. Schneider, K. Karube, T. Arima, Y. Taguchi, Y. Tokura, *Nano Lett.* **2022**, 22, 9358.
- [26] S. Seki, M. Suzuki, M. Ishibashi, R. Takagi, N. D. Khanh, Y. Shiota, K. Shibata, W. Koshibae, Y. Tokura, T. Ono, *Nat. Mater.* **2022**, 21, 181.
- [27] W. Legrand, J. Y. Chauleau, D. Maccariello, N. Reyren, S. Collin, K. Bouzehouane, N. Jaouen, V. Cros, A. Fert, *Sci. Adv.* **2018**, 4, aat0415.
- [28] I. Lemesch, G. S. D. Beach, *Phys. Rev. B* **2018**, 98, 104402.
- [29] R. D. Desautels, L. Debeer-Schmitt, S. A. Montoya, J. A. Borchers, S. G. Je, N. Tang, M. Y. Im, M. R. Fitzsimmons, E. E. Fullerton, D. A. Gilbert, *Phys. Rev. Mater.* **2019**, 3, 104406.
- [30] W. Li, I. Bykova, S. Zhang, G. Yu, R. Tomasello, M. Carpentieri, Y. Liu, Y. Guang, J. Gräfe, M. Weigand, D. M. Burn, G. van der Laan, T. Hesjedal, Z. Yan, J. Feng, C. Wan, J. Wei, X. Wang, X. Zhang, H. Xu, C. Guo, H. Wei, G. Finocchio, X. Han, G. Schütz, *Adv. Mater.* **2019**, 31, 1807683.
- [31] W. L. N. C. Liyanage, N. Tang, L. Quigley, J. A. Borchers, A. J. Grutter, B. B. Maranville, S. K. Sinha, N. Reyren, S. A. Montoya, E. E. Fullerton, L. Debeer-Schmitt, D. A. Gilbert, *Phys. Rev. B* **2023**, 107, 184412.
- [32] J. C. Slonczewski, *J. Appl. Phys.* **1973**, 44, 1759.
- [33] E. Schlömann, *J. Appl. Phys.* **1974**, 45, 369.
- [34] A. Hubert, *J. Appl. Phys.* **1975**, 46, 2276.
- [35] K. Karube, L. Peng, J. Masell, M. Hemmida, H. A. Krug von Nidda, I. Kézsmárki, X. Yu, Y. Tokura, Y. Taguchi, *Adv. Mater.* **2022**, 34, 2108770.
- [36] F. S. Yasin, J. Masell, K. Karube, D. Shindo, Y. Taguchi, Y. Tokura, X. Yu, *Nat. Commun.* **2023**, 14, 7094.
- [37] A. Aharoni, B. Heinrich, *IEEE Trans. Magn.* **1979**, 15, 1228.
- [38] C. Andreas, A. Kákay, R. Hertel, *Phys. Rev. B Condens. Matter Mater. Phys.* **2014**, 89, 134403.
- [39] R. Hertel, *J. Phys. Condens. Matter* **2016**, 28, 483002.
- [40] P. Milde, D. Köhler, J. Seidel, L. M. Eng, A. Bauer, A. Chacon, J. Kindervater, S. Mühlbauer, C. Pfleiderer, S. Buhbrandt, C. Schütte, A. Rosch, *Science* **2013**, 340, 1076.
- [41] A. Thiaville, J. M. García, R. Ditttrich, J. Miltat, T. Schrefl, *Phys. Rev. B Condens. Matter Mater. Phys.* **2003**, 67, 094410.
- [42] A. Hubert, *J. Magn. Magn. Mater.* **1975**, 2, 25.
- [43] C. J. Wang, P. Wang, Y. Zhou, W. Wang, F. Shi, J. Du, *npj Quantum Mater.* **2022**, 7, 78.
- [44] C. Donnelly, M. Guizar-Sicairos, V. Scagnoli, S. Gliga, M. Holler, J. Raabe, L. J. Heyderman, *Nature* **2017**, 547, 328.
- [45] M. T. Birch, D. Cortés-Ortuño, N. D. Khanh, S. Seki, A. Štefančíč, G. Balakrishnan, Y. Tokura, P. D. Hatton, *Commun. Phys.* **2021**, 4, 175.
- [46] G. Lai, T. Hirayama, A. Fukuhara, K. Ishizuka, T. Tanji, A. Tonomura, *J. Appl. Phys.* **1994**, 75, 4593.
- [47] S. J. Lade, D. Paganin, M. J. Morgan, *Opt. Commun.* **2005**, 253, 382.
- [48] C. Phatak, A. K. Petford-Long, M. De Graef, *Phys. Rev. Lett.* **2010**, 104, 253901.
- [49] N. Baba, K. Kaneko, M. Baba, *Sci. Rep.* **2020**, 10, 20146.
- [50] N. Baba, S. Hata, H. Saito, K. Kaneko, *Microscopy* **2022**, 72, 111.
- [51] L. Peng, K. V. Iakoubovskii, K. Karube, Y. Taguchi, Y. Tokura, X. Yu, *Adv. Sci.* **2022**, 9, 2202950.
- [52] T. Kawasaki, I. Matsui, T. Yoshida, T. Katsuta, S. Hayashi, T. Onai, T. Furutsu, K. Myochin, M. Numata, H. Mogaki, M. Gorai, T. Akashi, O. Kamimura, T. Matsuda, N. Osakabe, A. Tonomura, K. Kitazawa, *J. Electron Microsc.* **2000**, 49, 711.
- [53] K. Harada, A. Tonomura, Y. Togawa, T. Akashi, T. Matsuda, *Appl. Phys. Lett.* **2004**, 84, 3229.
- [54] A. Vansteenkiste, J. Leliaert, M. Dvornik, M. Helsen, F. Garcia-Sanchez, B. Van Waeyenberge, *AIP Adv.* **2014**, 4, 107133.
- [55] B. Berg, M. Lüscher, *Nucl. Phys. B* **1981**, 190, 412.